

Shallow Ambient-Noise 3D Tomography in the Concepción Basin, Chile: Implications for Low-Frequency Ground Motions

by Diego A. Inzunza, Gonzalo A. Montalva, Felipe Leyton, German Prieto, and Sergio Ruiz

Abstract Forecasting surface seismic intensities is the main objective of much of the research in seismic engineering. The seismic demand for tall buildings, bridges, wind farms, and other existing slender structures is predominantly at low frequencies, but these structures are usually outside the range of the design spectra prescribed by codes. This article presents a 3D tomography model of the Concepción basin, Chile, where the shear-wave velocity structure is estimated to 500-m depth. The maximum basin thickness is approximately 160 m, but the average is about 100 m. The underlying bedrock is composed of two different units. The interface between the two bedrock units, at a depth of about 460 m, causes a low-frequency resonance at 0.5 Hz. The two bedrock units have shear-wave velocities close to 1000 and 3700 m/s, respectively. The resonance in the neighborhood of 0.5 Hz is controlled by the thickness and V_S value of the first bedrock unit from roughly 100 to 460 m. This frequency coincides with the surface intensities recorded at the basin during the 2010 M_w 8.8 Maule earthquake. Shear-wave velocity (V_S) tomography models from dispersion curves show heterogeneities in half-space stiffness that predict the observed differences in low-frequency (long-period) ground motions.

Introduction

The Concepción basin is located in the center of the second most important metropolitan area in Chile. This alluvial basin was formed by the Biobío River and consists of a relatively homogeneous layer of sandy sediments (Montalva *et al.*, 2016).

The Concepción basin has historically been subjected to strong shaking by subduction zone earthquakes in 1570 (M_s 8.3), 1657 (M_s 8.0), and 1751 (M_w 8.5), which motivated the decision to move the city to its current location. The new location has experienced events of equal magnitude: 1835 (M_s 8.5), 1960 (M_s 8.5), and 2010 (M_w 8.8). The last event caused great damage to downtown Concepción and revealed the limited predictive capability of the Chilean national seismic regulations (Nch433 Of. 2009) for long-period ground motions. Site effects strongly affected seismic demand (Assimaki *et al.*, 2012; Montalva *et al.*, 2016) and often govern the damage distribution during large earthquakes, hence the need to characterize them appropriately. For this study, a 51-day ambient-noise survey was conducted in Concepción to assess the shear-wave velocity (V_S) structure of the basin and to study its relation to site effects (coordinate stations in Table 1).

Aki (1957) proposed the spatial autocorrelation (SPAC) technique that uses ambient-noise measurements to determine V_S structure. In his work, Aki shows that the ratio between the azimuthal average of the cross-spectral functions and the cross-spectra functions of a central reference sensor

corresponds to the first-order Bessel function, which can be used to obtain the Rayleigh-wave dispersion curve of a site. Chávez-García *et al.* (2005) generalized the SPAC method to different spatial configurations and combined frequency with time-domain correlograms to enrich the interpretation of the data. A large body of work on correlograms of microtremors allowed the development of seismic interferometry (e.g., Weaver and Lobkis, 2002; Snieder, 2004; Roux *et al.*, 2005; Sabra, Roux, and Kuperman, 2005). Seismic interferometry focuses on extracting the coherent component of microseisms among receivers from the average of the correlograms of their signals. Early studies using this technique conducted large-scale ambient-noise tomography (e.g., Moschetti *et al.*, 2007; Yang *et al.*, 2007). In this study, it is used to characterize the much smaller volume of the Concepción basin (e.g., Snelson *et al.*, 2007; Delorey and Vidale, 2011; Shirzad and Shomali, 2014a).

Previous qualitative uses of microtremors in Concepción include the work of Leyton *et al.* (2012) and Montalva *et al.* (2016), in which horizontal-to-vertical spectral ratios were successfully linked to damage after the 2010 event. Midorikawa *et al.* (2014), using SPAC characterized a V_S profile to a depth of 200 m, computed the amplification function, but it did not fully capture the observed response spectra at the Concepción strong-motion station (CONC) during the 2010 Maule earthquake.

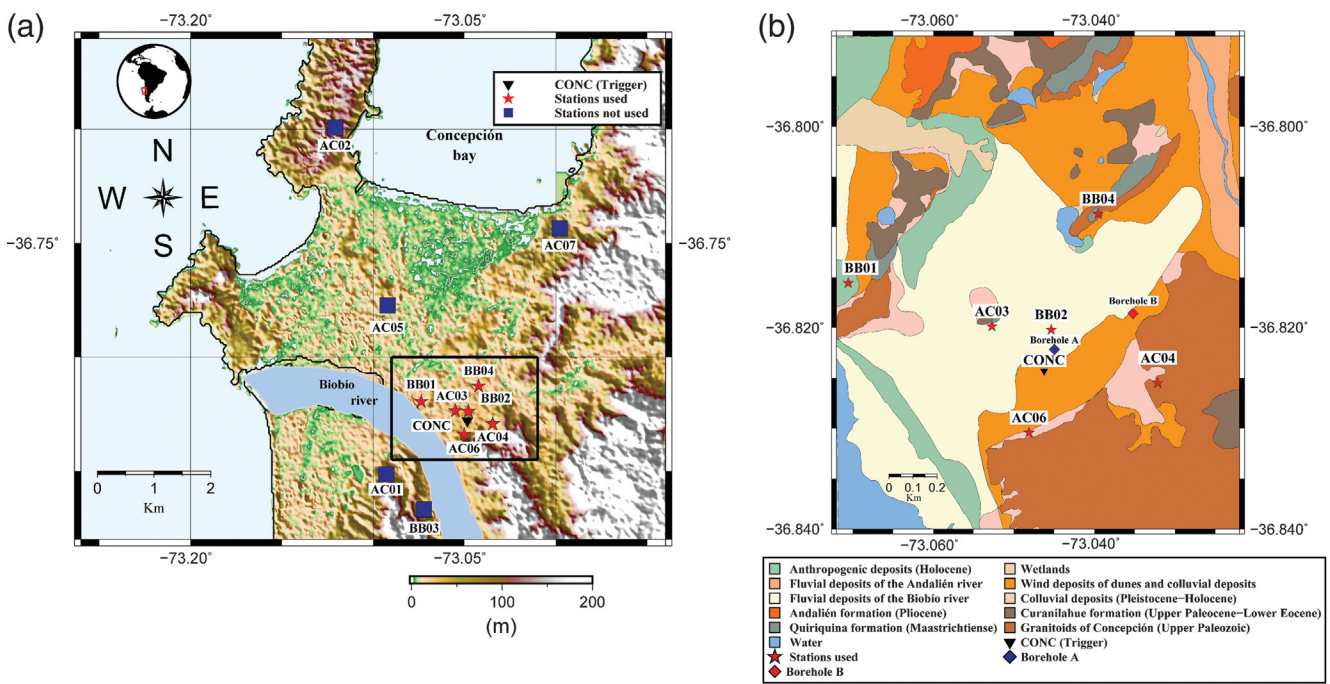


Figure 1. (a) Metropolitan Concepción: the black box contains the stations used. The triangle represents CONC station (triggered), stars represent stations used for tomography, and squares represent unused stations. (b) Geologic map and station locations within the Concepción basin.

This work uses the results of a temporary seismic network of 13 broadband and accelerometer stations deployed in the Concepción metropolitan area. It focuses on six of these stations located in and around the Concepción basin. Time-domain correlograms and cross-spectra functions are calculated, and the resulting dispersion data were combined. This allows the characterization of the dispersion curve over a broader frequency range. The information is used to compute 1D site amplification functions that include not only sediments overlying a half space, but the velocity structure is also defined to a depth of 500 m, which in this case includes two bedrock layers affecting the Concepción basin.

The results are then compared with the recorded ground motions at CONC.

The travel-time tomography models consider only downtown Concepción (Fig. 1). As shown by Cabas (2016), the assumption of homogeneity of the half space at the base of a soil profile is not always realistic and can have significant implications. This assumption is tested for the case of Concepción using a 3D model of V_S to a depth of 500 m.

Location

The Concepción basin (Fig. 1a) is located along the coast of south-central Chile. The sediments in the basin are primarily sands and silty sands deposited by the Biobío River. The geological map of Concepción (Vivallos *et al.*, 2010, Fig. 1b) shows Pleistocene to Holocene alluvial deposits under downtown Concepción. Galli (1967) showed the basin is underlain by a weathered granite, chiefly tonalities. V_S measurements of tonalites from the “El Teniente” mine (located roughly 120 km south of Santiago, Chile) by Rojas (2014) show V_S values in the order of 3200 m/s at depths of 350 m.

The Concepción basin is typically less than 100 m thick. Poblete and Dobry (1968) reported that bedrock formed of granite rock appears at a depth of about 100 m in a borehole near the eastern margin of the basin (Fig. 1b, borehole A). The inversion of gravity data by Montalva *et al.* (2016) using the data collected by Vivallos *et al.* (2010) confirmed this depth and estimated that the basin depth varies from zero (outcropping rock) to about 160 m. This inversion was confirmed by a recent 80-m-deep borehole drilled for the

Table 1
Geographical Coordinate Stations

Station	Latitude (°)	Longitude (°)
Accelerometer 01	−36.851323	−73.092869
Accelerometer 02	−36.699158	−73.120811
Accelerometer 03	−36.823575	−73.055062
Accelerometer 04	−36.829245	−73.034579
Accelerometer 05	−36.777340	−73.092168
Accelerometer 06	−36.833860	−73.050231
Accelerometer 07	−36.743539	−72.997855
Broadband 01	−36.819570	−73.073752
Broadband 02	−36.823780	−73.047889
Broadband 03	−36.866753	−73.072227
Broadband 04	−36.812755	−73.042261
Borehole A	−36.822183	−73.044958
Borehole B	−36.818595	−73.035214

“Site Effects Observatory on Alluvial Basins” project at another location within the basin (Fig. 1b, borehole B).

Methodology

The thickness of the Concepción basin varies from 0 to 160 m and is typically less than 100 m. Dispersion curves of the bedrock and sediments beneath downtown Concepción were estimated based on the microtremor records of the field campaign. This procedure used correlograms in the temporal domain and cross spectra in the spectral domain. Time-domain correlograms between pairs of microtremors records were computed for the six stations within the basin. The correlograms of microtremors between two stations are described by [Sabra, Gerstoft, et al. \(2005\)](#) as:

$$C_{ij}(r_1, r_2, \tau) = \int_0^T \nu_i(r_1; t) \nu_j(r_2; t + \tau) dt, \quad (1)$$

in which t is the time; $\nu_i(r_1; t)$ and $\nu_j(r_2; t)$ are the recorded microtremors in the positions r_1 and r_2 , respectively; T is the length of the time window; $C_{ij}(r_1, r_2, \tau)$ is the correlogram; and τ is the time lag. [Sabra, Gerstoft, et al. \(2005\)](#) demonstrated that the temporal derivatives of the correlograms are approximations to the velocity Green's functions, hence

$$\frac{dC_{ij}}{dt} \approx -G_{ij}(r_1; r_2, t) + G_{ji}(r_2; r_1, -t), \quad (2)$$

in which $G_{ij}(r_1; r_2, t)$ is the velocity Green's functions between two locations. [Sabra, Gerstoft, et al. \(2005\)](#) showed that when the Green's function is not interpreted, it is not necessary to take the derivative; hence, the correlograms are used directly. The method used for processing the data is similar to the one described by [Bensen et al. \(2007\)](#), which compiles different methodologies. Only the vertical component of the data was used, with the mean, trend, and instrument response removed. The sampling frequency was reduced to 10 Hz to decrease the computation time; this simplification does not cause problems because the range of frequencies studied is 0.4–1.5 Hz. Windows of 600-s length were selected, a 5% cosine taper was applied to each trace, and a four-pole Butterworth bandpass filter with a $\pm 15\%$ width from the central frequency was applied. To achieve more homogeneous signals and reduce the effects of transients, the temporal (1 bit; [Larose et al., 2004](#)) and spectral normalization of the traces ([Shapiro et al., 2006](#)) were carried out.

Correlograms with group velocities between 0.3 and 3.5 (km/s) were selected because they are the range where most velocities are found in the histograms as shown in Figure 2. The signal-to-noise ratio (SNR) was calculated using the [Shirzad and Shomali \(2014b\)](#) method. Correlograms having SNR greater than 2 were selected. Finally, an average of 912 correlograms was used for each path, which were then stacked.

The group velocities were integrated as shown in equation (3) to obtain the phase velocity, in which S_p and S_u are phase and group slowness, respectively; ω is the angular

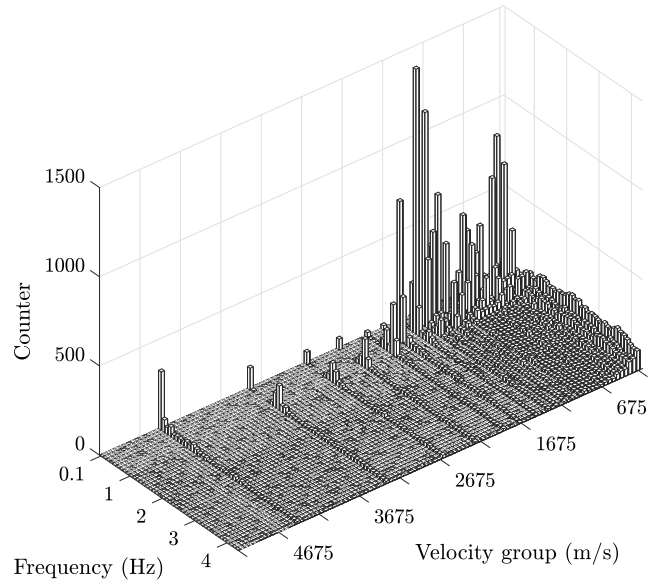


Figure 2. Histogram of group velocity between all stations.

frequency; and S_c^n is a known value of the phase slowness with its corresponding associated frequency ω_n :

$$S_p(\omega) = \omega^{-1} \left(\int_{\omega_n}^{\omega} S_u(\omega) d\omega + \omega_n S_c^n \right). \quad (3)$$

The cross spectra were calculated in the spectral domain to calculate the Rayleigh-wave phase velocity. The [Chávez-García et al. \(2005\)](#) methodology was used to estimate the first-order Bessel's function J_0 as:

$$\bar{\rho}(r, \omega) = J_0 \left(\frac{\omega \times r}{c(\omega)} \right), \quad (4)$$

in which $\bar{\rho}$ is the azimuth average of the cross-spectra coefficient.

[Ekström et al. \(2009\)](#) proposed that when computing the mean of the cross-spectra functions between a pair of stations, the functions will not always have the behavior of the first-order Bessel's functions, but the zero crossing will retain these characteristics; hence at these points, the phase velocity can be computed through the argument of the Bessel's functions using the following equation:

$$C(\omega_0) = \frac{\omega_0 \times r}{Z_n}, \quad (5)$$

in which $C(\omega_0)$ is the phase velocity, ω_0 is the angular frequency in which the Bessel's function is zero, r is the interstation distance, and Z_n is the n th zero crossing in the Bessel's function.

The time-domain phase velocities have been complemented with those calculated in the spectral domain to improve the characterization of the dispersion curve. Figure 3 shows the dispersion curve between stations BB01 and BB04 using both time and frequency domains. An inversion of the dispersion curves was carried out to construct a tomography

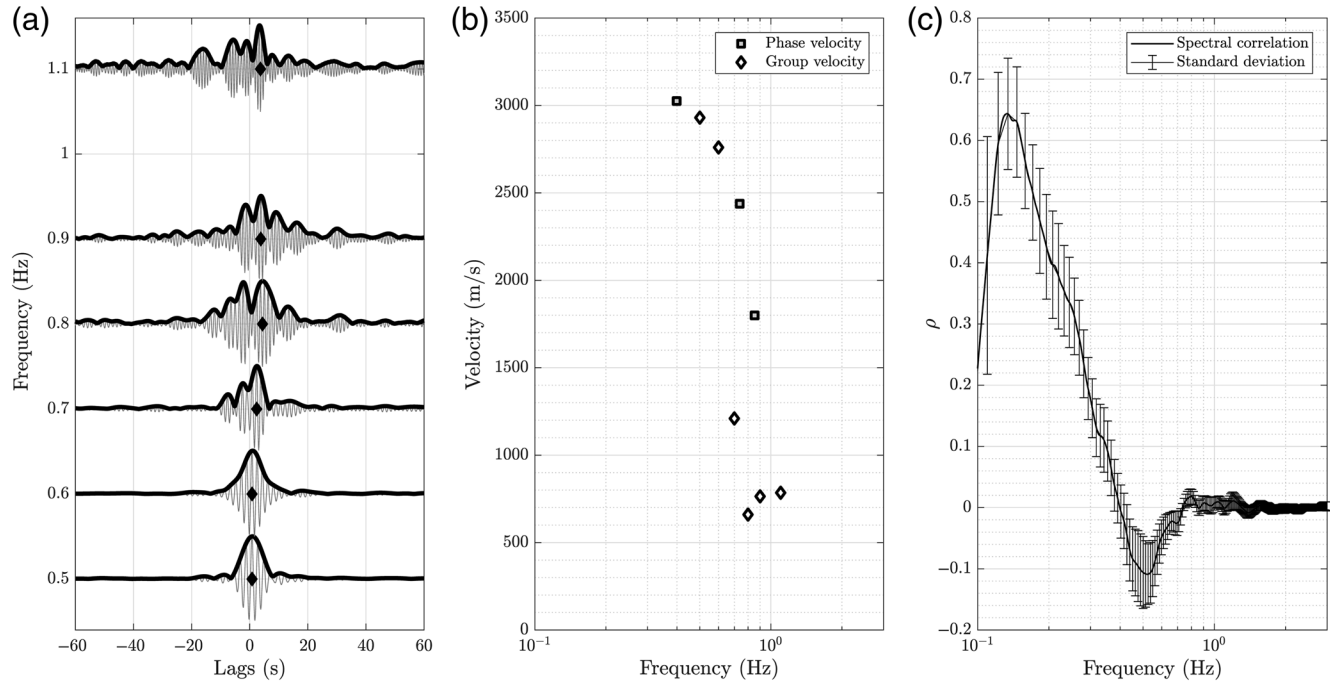


Figure 3. Dispersion curve between stations BB01 and BB04. (a) Stacked correlograms of 51 days, envelopes (thick line), and black diamonds mark the envelope's maximum amplitude time lag. (b) Group velocity from correlograms and phase velocity using Ekström *et al.* (2009). (c) Cross-spectra function with zero crossings.

model for V_S . The problem starts from the integral of the travel times (t) for a given slowness S along a ray path; this is expressed in the equation (6), in which dl is the differential line element along the ray path

$$t(l) = \int_{\text{ray path}} S(l)dl, \quad (6)$$

which can be expressed in its discrete matrix form as indicated in equation (7). This is the fundamental relation to find, in which \mathbf{L} is the run-length matrix of each ray path for each cell that is crossed, \mathbf{S} is the slowness matrix to find, and t is travel time for each ray (i.e., the travel-time length between two points divided by the phase velocity estimated from the dispersion curve):

$$\mathbf{L} \times \mathbf{S} = t, \quad (7)$$

$$\mathbf{L}^T \mathbf{L} \mathbf{S} = \mathbf{L}^T t, \quad (8)$$

$$\begin{aligned} f(\mathbf{S}) &= \underbrace{\frac{1}{2}(\mathbf{L}\mathbf{S} - t)^T(\mathbf{L}\mathbf{S} - t)}_{\text{misfit function}} + \underbrace{\frac{\eta^2}{2}\mathbf{S}^T\mathbf{S}}_{\text{penalty function}} \\ &= \underbrace{\frac{1}{2}\mathbf{S}^T\mathbf{L}^T\mathbf{L}\mathbf{S} - t^T\mathbf{L}\mathbf{S} + \frac{1}{2}t^T t}_{\text{misfit function}} + \underbrace{\frac{\eta^2}{2}\mathbf{S}^T\mathbf{S}}_{\text{penalty function}}, \quad (9) \end{aligned}$$

$$\Delta f(\mathbf{S}) = \mathbf{L}^T(\mathbf{L}\mathbf{S} - t) + \eta^2\mathbf{S}, \quad (10)$$

$$\min f(\mathbf{S}^k - \alpha\Delta\mathbf{S}^k). \quad (11)$$

To build a tomography model, a system of equations must be solved to find the unknown slowness S_i constant for each cell i . Considering the ray path is velocity dependent (i.e., the inversion process is a nonlinear one), to keep tomographic studies for shallow seismic surveys within linear bounds, a bias of a few percent in the estimated models due to the simplified linear approach can be accepted (Kugler *et al.*, 2007). The analysis assumes linear ray theory by assuming that the velocity model varies smoothly over the distance of a wavelength. The process is still a nonlinear iterative method because the travel times are recalculated for each ray path until the misfit is minimized. For an overdetermined system (restrictions greater than unknowns) as in this case, the solution of slowness (\mathbf{S}) that satisfies the system of normal equations, shown in equation (8), must be found. The solution to the system of normal equations using a misfit function coincides with the solution that minimizes the quadratic function shown in equation (9). The gradient is therefore given by equation (10). The conjugate gradient method shown in equation (11) was implemented to solve the problem, in which α is the search line and Δs is the gradient. The penalty function shown in equation (9) was introduced because the number of Hessian (H) conditions is large ($H = \mathbf{L}^T\mathbf{L}$). Several different models of slowness can predict the same data. To fix this problem, restrictions were added to keep the solution close to the origin, and the term η was given the value of 0.1; this value was determined using a trade-off curve.

The initial tomography model was built from an interpolation of V_S profiles using the Picozzi *et al.* (2009) method

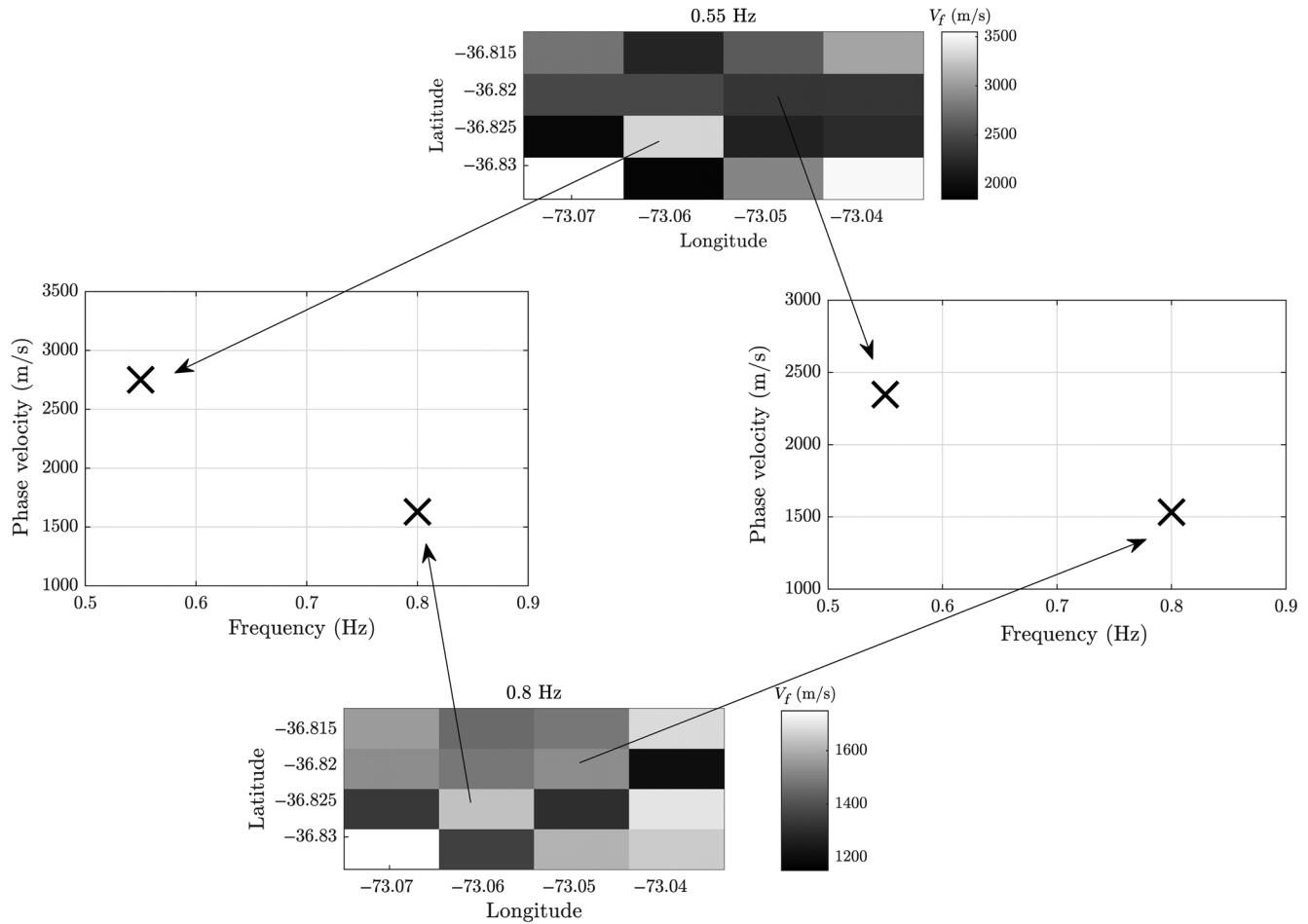


Figure 4. Values of phase velocity for each cell from travel times at each frequency.

as implemented in other studies (Hannemann *et al.*, 2014; Cheng *et al.*, 2015; Szanyi *et al.*, 2016). The idea is to incorporate the constraints on the system indicated in equation (7) and solve by minimizing the difference between observed and calculated travel times as shown in equation (12), in which $\Delta t^{(k)}$ is the normalized difference between observed and calculated travel times and $[t_0 - t_c]/t_o$, $\Delta S^{(k)}$ is the normalized difference between the slowness for the k th iteration $[S^{(k)} - S^{(k-1)}]/S^{(k)}$. The process starts from the slowness of the homogeneous first model $S^{(k=1)}$, which are obtained from a linear fit between the observed travel times and the interstation distances. The mean of these slowness values was used in the model and initial travel times $t^{(k=1)}$ were then computed using equation (7). The new solution $S^{(k+1)}$ was obtained solving equation (12)

$$W\Delta t^{(k)} = L_2\Delta S^{(k)}, \quad (12)$$

$$L_2 = \begin{bmatrix} \mathbf{W}L_1 \\ \mathbf{K}\delta^2\mathbf{M} \end{bmatrix}, \quad (13)$$

in which \mathbf{W} is an $m \times m$ diagonal matrix (Tukey, 1974) used to stabilize the iteration process and is made up of weighting

factor elements defined by the adaptive biweight estimation method. L_2 incorporates the constraints, as shown in equation (11). The upper part shows the $m \times n$ L_1 matrix, which is the longitude matrix indicated in equation (7), in which m is the number of rays and n is the number of cells. In the lower part of matrix L_2 (see equation 13), the $n \times n$ submatrix \mathbf{K} indicates the number of rays that cross the cell times the cell's ellipticity (Kissling, 1988). This term is calculated by dividing each cell into four quadrants and assigning to each quadrant the distance of the rays that cross it by constructing a ray density matrix, as is also the case of the matrix \mathbf{L} in equation (7). Then singular values for each cell are computed (λ_1 , λ_2), and finally the ellipticity is calculated as λ_1/λ_2 . δ^2 is the damping factor of the model, which was determined to be 0.5 using trial and error, which as indicated by Long and Kocaoglu (2001) aims to stabilize the inversion process. The $n \times n$ submatrix \mathbf{M} is used to smooth the results in the horizontal plane.

Solving equation (10) for several frequency ranges allows the computation of dispersion curves for each cell as shown in Figure 4 (Brenguier *et al.*, 2007). The V_S profiles are obtained by inverting the dispersion curves using Dinver (Wathelet, 2008), which implements the neighborhood

algorithm as proposed by [Sambridge \(1999\)](#). These profiles are then interpolated, and a V_S tomography model is obtained.

The second model computes the 3D V_S tomography model in one step as it was proposed by [Pilz et al. \(2012\)](#). This method has been implemented by [Hannemann et al. \(2012\)](#) and [Amoroso et al. \(2017\)](#). A large part of this second method uses stages (or equations) of the previously presented tomography model to minimize the difference between observed and calculated travel times as shown in equation (12). The difference of this more direct method is that the range of the calculated matrix increases and carries a higher computational cost. The vector $\Delta t^{(k)}$ is $r \times f$ long, in which r is the number of rays and f is the number of frequencies used. $\Delta S^{(k)}$ is the $m \times n$ difference of slowness, in which m is the number of cells per layer and n is the number of layers.

Matrix \mathbf{L}_2 (in equations 12 and 13) is composed of the $rf \times mn$ \mathbf{L}_1 matrix in the upper part and by the $mnf \times mnf$ \mathbf{K} matrix in the lower part. The \mathbf{K} submatrix is the product of two functions, the first (equation 14) is the same as in the previous method, and the second depends on the vertical coordinates (equation 15). This second function is calculated using the analytic solution for the vertical displacement ([Hill, 2010](#)) and is shown in the following equation:

$$u_3(z) = me^{mkz} - se^{pkz}, \quad (14)$$

in which $z < 0$, k is the wavenumber, $m = 0.8475$, $p = 0.3933$, and $s = 1.4679$. The final value of the second function (w) is determined by normalizing average value of u_3 within each layer as

$$w = \frac{\int_{d_1}^{d_2} u_3 dz}{\int_0^\infty u_3 dz}, \quad (15)$$

in which d_1 and d_2 are the lower and upper bounds of each layer.

The $mnf \times mn$ \mathbf{M} matrix, described by [Ammon and Vidale \(1993\)](#), was not used in this study because one of the objectives was to identify strong impedance contrasts. Equation (12) allows the computation of each cell's phase slowness (here, cell is referred to as the entire height of the model on each horizontal division). Considering a Poisson module between 0.2 and 0.4, the relation between the slowness (S) and V_S is expressed by equation (16), in which $C = 0.92$. The final V_S tomography model in the second approach was calculated by solving for the V_S value in the following equation:

$$S = \frac{1}{CV_S}. \quad (16)$$

The values of V_S in the tomography maps are interpolated using kriging ([Oliver and Webster, 2015](#)).

Results and Discussions

The dispersion curve, characterized at frequencies from 0.4 to 1.5 Hz, allowed the inversion of the shear-wave veloc-

ity structure for depths up to 500 m. The time-domain processing of the ambient noise shows information in a wider range of frequencies than the spectral domain, as also observed by [Chávez-García and Rodríguez \(2007\)](#).

The analysis focused on the Concepción downtown where the Maule earthquake was recorded at CONC (Fig. 1b), a triggered permanent station. It used stations BB01, BB02, BB04, AC03, AC04, and AC06, with interstation distances from 0.64 to 3.65 km. The dispersion curves for the area are shown in Figure 5a, which are complemented at higher frequencies using the phase velocities calculated by [Montalva et al. \(2016\)](#) and using the SPAC technique, with both sets of data merging into a continuous dispersion curve, as one would expect from compatible data sets.

Two bedrock layers (bedrock units I and II) can be identified below the basin sediments. A first approximation for the V_S profile in the basin was made using the fitted dispersion curve through ordinary least-squares shown in Figure 5a and then inverting it using the neighborhood algorithm ([Wathelet, 2008](#); Fig. 5b). The inverted profile has three significant layers (see Table 2), showing two abrupt V_S changes at 93 and 464 m.

Figure 6a shows the transfer function (TF) calculated following the 1D elastic wave propagation theory ([Thomson, 1950](#)) and using only the V_S values. The Q -value used for each layer followed the relation $Q = V_S/10$ ([Midorikawa et al., 2014](#)). Unlike the three-layer model, the two-layer model in Figure 6a fails to produce a peak close to 0.5 Hz. Hence, it is postulated that the 0.5-Hz peak can be attributed to the second—and deeper—impedance contrast.

Using the 5% damped pseudospectral acceleration recorded at CONC for the Maule event as a reference (Fig. 6b), the three-layer TF explains the peak close to 0.5 Hz. However, the function does not explain the peak near 0.67 Hz that the transverse spectrum shows. This may be because of several reasons such as that the inverted dispersion curve is an average of the measured points (Fig. 5a) or that 3D effects are relevant in the response.

Tomography

The 1D analysis performed is able to explain the low-frequency response observed at 0.5 Hz in the CONC station, and it should be noted that this is the only station that showed a strong spectral acceleration (SA) value at this low frequency for the 2010 Maule earthquake ([Bastías and Montalva, 2016](#)). However, this still does not explain the difference in the horizontal response spectra at CONC station. The tomography of the basin explained earlier is used to shed light into this difference.

The experiment used the six stations in downtown Concepción with 15 ray paths (Fig. 7a). A 4×4 grid with 15 effective cells was used; each cell was 872 m in latitude and 587 m in longitude with layer interfaces at 0, 60, 100, 150, 200, 300, 400, and 500 m. The first 3D model implemented from interpolation of individual V_S profiles is shown

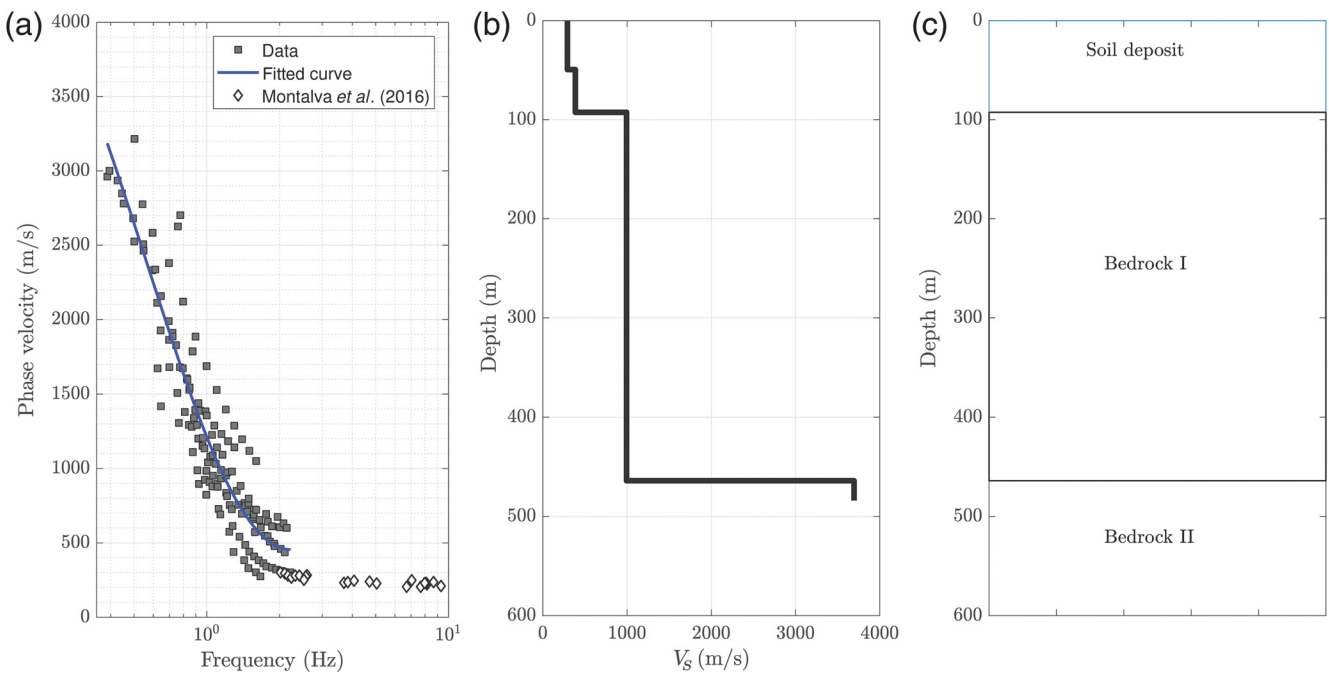


Figure 5. (a) Dispersion curves data for downtown stations BB01, BB02, BB04, AC03, AC04, and AC06; (b) V_S profile; and (c) physical model interpreted from the profile.

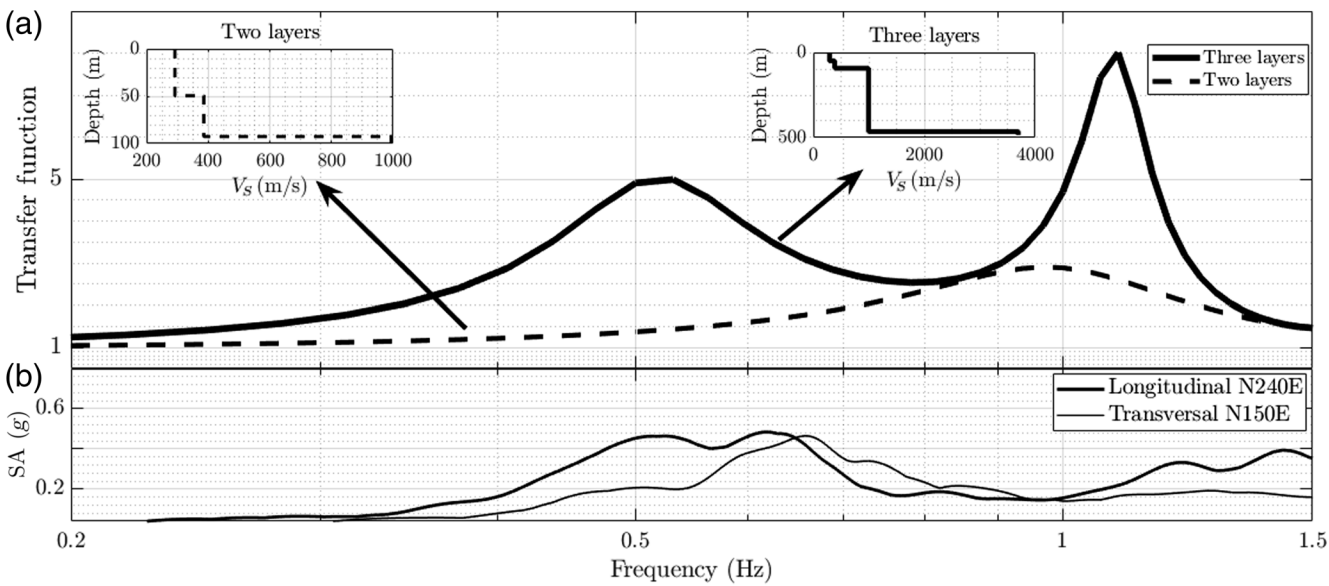


Figure 6. (a) Transfer functions (TFs) for two and three layer profiles. (b) Horizontal response spectra at the CONC station for the 2010 Maule earthquake.

Table 2
 V_S Profile

Layer (m)		V_S (m/s)
Start	End	
0	49	292
49	93	386
93	464	993
464	—	3695

in Figure 7, where phase slowness maps (Fig. 7a) are made for frequencies 0.55, 0.8, 1.0, and 1.5 Hz. For the 1.0- and 1.5-Hz frequencies, some cells were not crossed by ray paths; in these cases, the information on the dispersion curve was complemented with microtremors measurements at local scale previously processed by Montalva et al. (2016).

The dispersion curves for every cell were inverted, obtaining a shear-wave velocity profile for each cell (15 in total). These profiles are interpolated resulting in the model

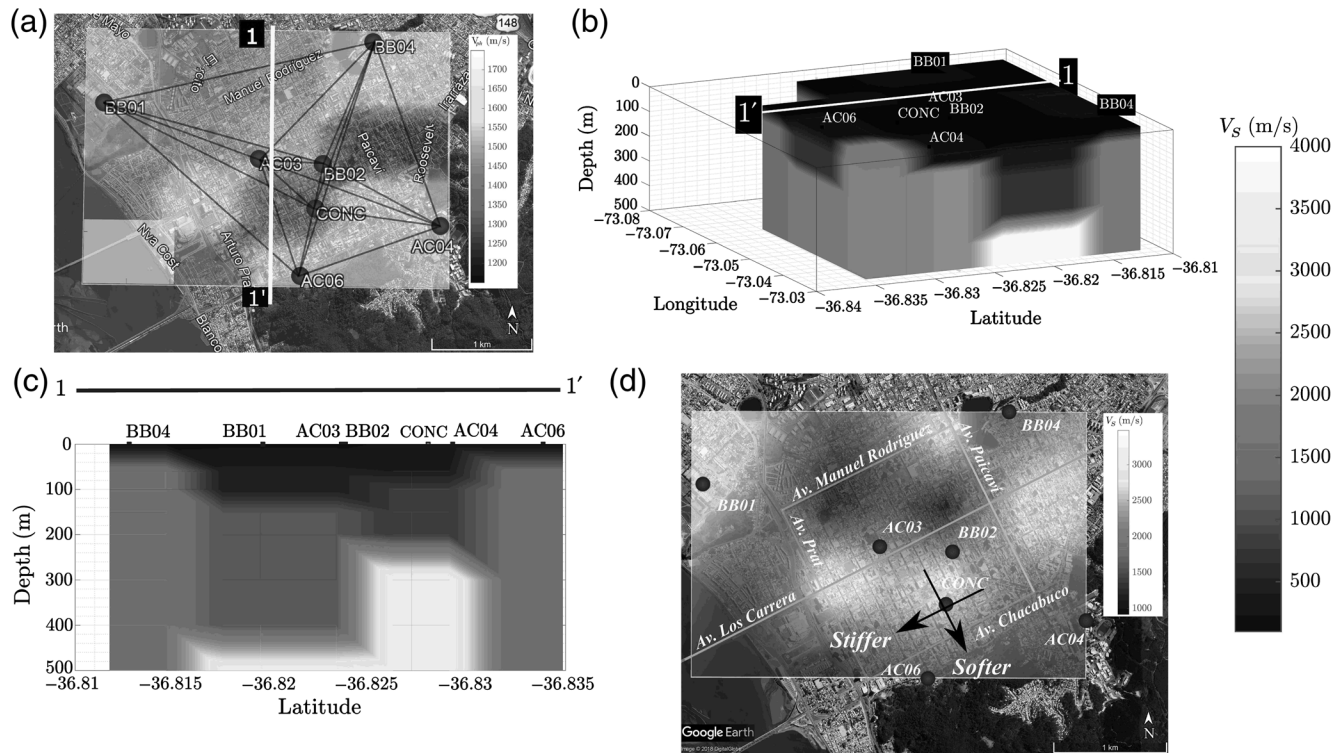


Figure 7. Tomography model from interpolated profiles. (a) Phase velocity map for 0.8 Hz, (b) 3D model down to a depth of 500 m, (c) cross section at 1–1', and (d) plan view at a depth of 400 m; the gray lines show major roads. The color scale in (d) was changed to highlight velocity changes in the depth slice. Black arrows show the directions of different stiffness associated with different seismic demand.

presented in Figure 7b. A cross section through the model is presented in Figure 7c. In the first 150 m, the shape of the basin is shown with varying sediment thickness; below this, the bedrock unit I layer is observed with shear-wave velocities around 1000 m/s. Finally, between 300 and 400 m bedrock, unit II layer appears, which is the layer that causes the amplification at low frequencies (i.e., 0.5 Hz).

The second tomographic model, which obtains the 3D V_s model developed in one step from the Rayleigh-wave travel times, is shown in Figure 8. The depth limits for the layers were 0, 60, 100, 150, 200, 300, 400, and 500 m. Frequencies 2.2, 2.0, 1.8, 1.5, 1.2, 1.0, and 0.9 Hz are used, obtaining the final model after iteration 98. Cross sections through the model, presented in Figure 8b,c, show the 150 m of sediment. Under the sediment layer, the first bedrock unit I layer has velocities close to 1000 m/s, along with the second bedrock unit between 400 and 500 m with velocities around 2500 m/s. This is the difference between the two models. The computational time of the second tomography model is 10 times the first model because of the range of matrices to be resolved. The V_s profiles interpolation model produces V_s variations at large depths that are compatible with the different surface response in the longitudinal and transverse directions (Fig. 7d). This spatial variability is less evident in the one-step model.

Although the second bedrock unit does not appear at the same depth in both models, the 1D TF for both models at

CONC has a strong amplification close to 0.5 Hz, as shown in Figure 9. This suggests that the 0.5-Hz peak (in the CONC spectra) is controlled by a structure deeper than the basin sediments.

Three TFs are shown in Figure 9. The first results from the curve fitted to the point cloud in Figure 5a and the inversion of that dispersion curve. The second and third results show that TFs shown in Figure 9 were computed from 1D profiles at CONC location taken from each of the tomography models. Figure 9 also shows that the different TFs change somewhat significantly in high frequencies; however, the low-frequency peak that was the objective of the model is present in all of them. This is expected because although changes in bedrock V_s can have a strong impact on surface intensities, in this case, the impedance contrast is large in all three cases. Therefore, the TF changes mainly in amplitude. The functions provide a reasonable explanation for the longitudinal spectrum of the 2010 Maule earthquake ground motion recorded at CONC, which is located in the deeper zone of the basin. Although the intent of this article is not to compare tomographic methods, the V_s interpolation method best captures the surface response at 0.5 Hz as well as the variation between longitudinal and transverse components. There is insufficient evidence to say which method is better, but in this case, the V_s interpolation fits the observations better.

Because the depth to the bedrock unit I layer or the base of the sediment has the shape of a Mexican hat (see Montalva

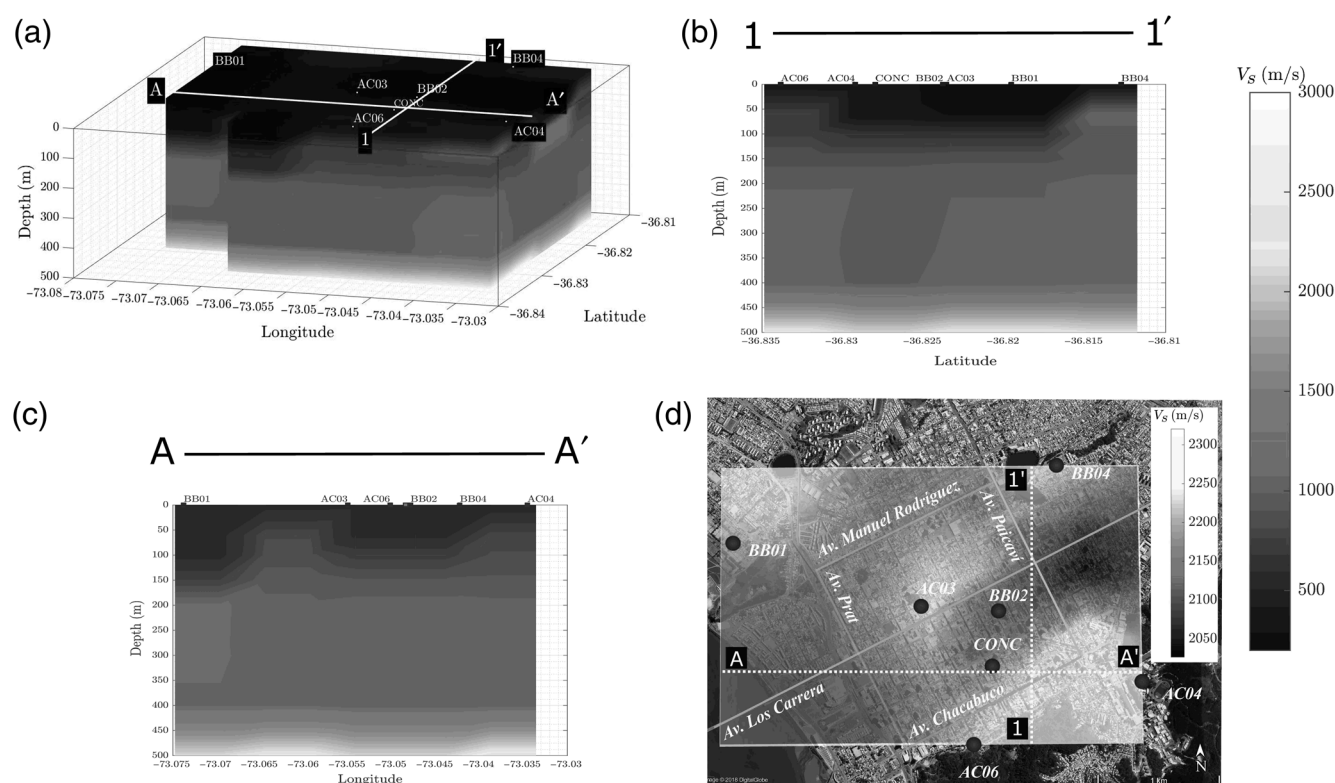


Figure 8. One-step tomography model. (a) 3D model up to a depth of 500 m, (b) cross-section view 1–1', (c) cross-section view A–A', and (d) V_S map at a depth of 500 m; gray lines show major roads. The color scale in (d) was changed to highlight velocity changes in the depth slice.

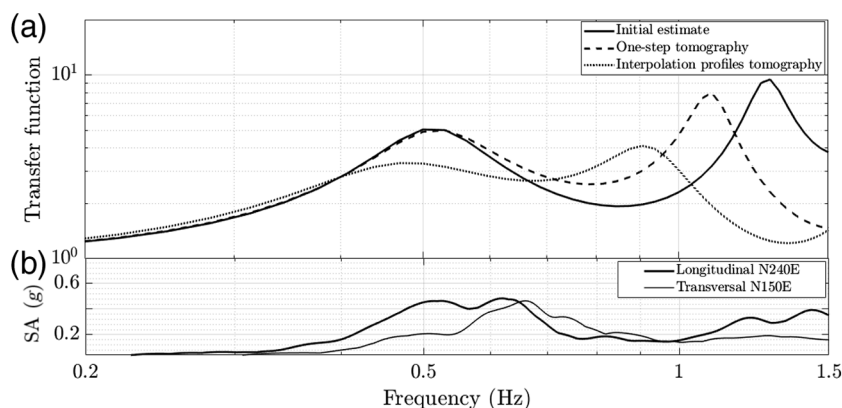


Figure 9. (a) TFs at CONC station. Continuous line represents the global dispersion curve adjusted to the point cloud as an initial estimate. Dashed line represents the V_S profile taken from the one-step tomography model. Dotted line represents the V_S profile from the interpolated profiles tomography. (b) Horizontal response spectra at the CONC station for the 2010 Maule earthquake.

et al., 2016), basin margin effects (e.g., Pilz *et al.*, 2011) contribute to the surface response. This makes surface intensity and damage variable despite a unique site class according to the Chilean and U.S. seismic codes.

An azimuthal analysis of the horizontal spectra at the CONC station is shown in Figure 10, where the spectra are computed for every rotation angle, and the three shown

(RotD00, RotD50, and RotD100) are the 0th, 50th, and 100th percentiles of the SA azimuthal analysis for each frequency (or period). The longitudinal spectrum closely matches the maximum azimuthal value, which suggests that the heterogeneity of the half space could partly explain the difference between the longitudinal and transverse spectra. For this hypothesis to hold true, the impedance contrast would need to be greater in the longitudinal direction. This is the case and is shown by arrows in Figure 7d.

Average shear-wave velocities are calculated for the area of two ellipses centered at CONC (-36.83° , -73.05°), with major axes in the longitudinal and transverse directions, respectively. The V_S values are taken from the 3D tomography

at 400 m, where the bedrock unit II layer begins. The ellipses dimensions are 95.2 m for the semiminor axis and 726.1 m for the semimajor axis, as shown in Figure 11a. The azimuthal average values of V_S (i.e., rotating the ellipses) are shown in Figure 11b. Higher V_S values were observed close to the east–west direction axes and lower than the north–south axes. The same analysis was performed for the

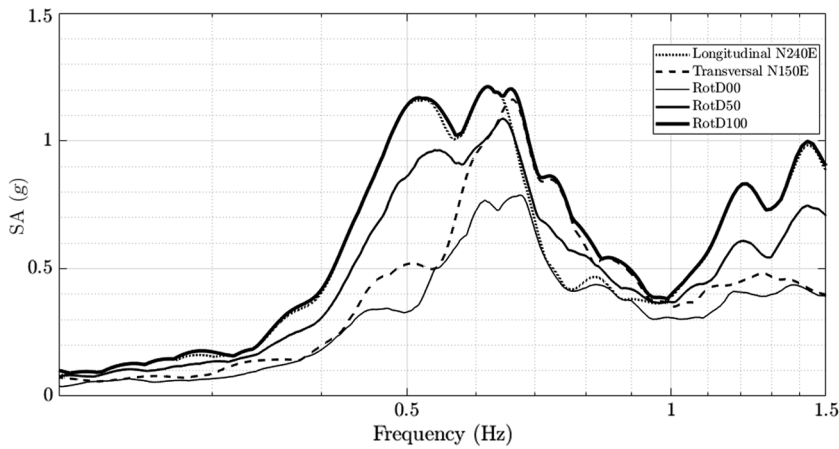


Figure 10. Response spectra for as-recorded and rotated horizontal components of the CONC station records for the 2010 Maule earthquake.

shallower depths of the model. With the averaged V_S values from surface to the depth of the second impedance contrast, the TF was calculated for the longitudinal and transverse directions recorded at CONC station, as shown in Figure 11c. Although the TF of the actual record is not available, one can observe the relation between the computed TF and the spectrum for the recorded ground motion.

Ruiz and Saragoni (2009) discussed the spectral peaks of several strong ground-motion records, including Mexico City (1985) and Valparaíso (1985). They postulate that when there is more than one peak in the spectrum, the first one is associated with the seismic source, and the second one is associated with the vibration of the soil deposits. In this work, it is proposed that the second peak is attributable to site effects (i.e., soil and bedrock layers). In seismic hazard analyses, site effects are typically considered via V_S profiles that end in a homogeneous half space (Cabas, 2016), but as it has been shown in this case, this simplification might not be

accurate and may have significant impacts on surface ground motions.

Conclusions

The shear-wave velocity structure for downtown Concepción was estimated to a depth of 500 m using ambient-noise dispersion curves from 0.4 to 1.5 Hz. Three layers were identified: (1) a thin veneer of alluvial deposits fills the basin of about 100 m, (2) this overlays a bedrock unit, and (3) another bedrock unit is identified at a depth of 464 m. The impedance contrast between the two bedrock units causes a low-frequency resonance at about 0.5 Hz.

The two tomography models presented here show differences in the V_S values calculated for these bedrock layers, showing that there is epistemic uncertainty in these methods (i.e., same data can produce different V_S estimates). However, despite these differences, the V_S structure shows these two bedrock units in both models. The V_S of bedrock unit II is consistent with unweathered tonalites as expected from the geologic map pattern in Figure 1b. The V_S of bedrock unit II may represent weathered rock units, likely tonalites.

The high-seismic demand near 0.5 Hz observed at station CONC for the Maule earthquake cannot be explained by a homogeneous half space. The V_S tomography allowed the estimation of deeper V_S profiles even while using a 1D-type analysis, and it explains the 0.5-Hz peak of the recorded ground-motion spectra. Therefore, a deep (500 m in this case) velocity structure would be necessary to explain these low-frequency amplifications. The proposed TFs explain the observed spectra at CONC station for both longitudinal

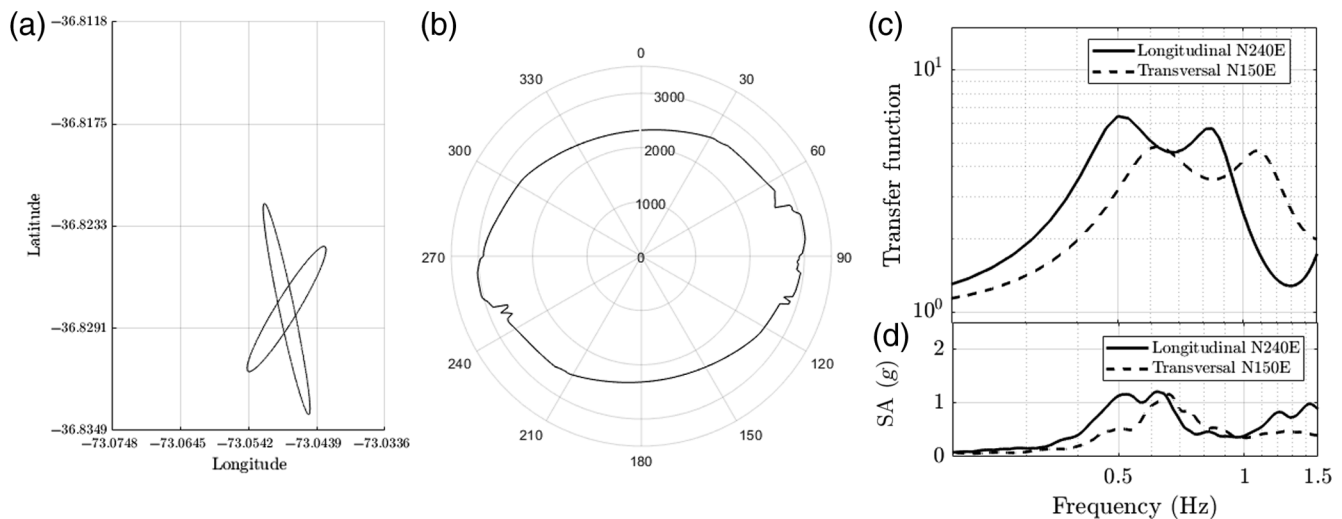


Figure 11. Ellipse rotation. (a) Ellipse position, (b) azimuthal V_S averaged values at a depth of 400 m, (c) TFs of averaged V_S in longitudinal and transverse directions, and (d) horizontal response spectra at the CONC station for the 2010 Maule earthquake.

(0.5 Hz) and transverse (0.67 Hz) peaks. The results highlight the importance and difficulty of selecting the half space in site-response studies. The choice will modify the surface demand estimates (in this case, for low frequencies). A linear analysis incorporating information of impedance contrasts at greater depths is appropriate to improve surface seismic estimation.

The assumption of a homogeneous half space would be erroneous for the Concepción basin. A higher resolution study using more stations is currently being conducted by the research group to further validate this finding.

Data and Resources

The data used for this investigation are passive records from continuous ambient-noise measurements from two field campaigns in the metropolitan area of Concepción, Chile. These data are available upon request from the authors. The first campaign used two Trillium 120 broadband stations from Nanometrics, configured to a sampling frequency of 200 Hz and monitored for 54 days in the months of November and December 2014. The second campaign used 11 stations that were deployed as illustrated in Figure 1. Seven Meridian Compact PH Nanometrics accelerometers and four CMG-3T Güralp broadband were installed. These instruments have a fundamental period of 120 s and a sampling frequency of 100 Hz. The instruments were buried, whenever possible, and located as far away from anthropogenic influence as possible within a large city.

Acknowledgments

This work was partly funded by Fondo Nacional de Desarrollo Científico y Tecnológico (FONDECYT) Award Number 11121404 and the Millennium Nucleus “The Seismic Cycle Along Subduction Zones” (CYCLO), Millennium Scientific Initiative (MSI) of the Chilean Government Grant Number NC160025. Data gathered with the Fondecyt EQM160015 project “Site Effects Observatory on Alluvial Basins” were also instrumental. All maps were generated with the Generic Mapping Tools (GMT; Wessel *et al.*, 2013). The authors would like to thank the Geopsy team (www.geopsy.org, last accessed January 2018) for making its software available.

References

- Aki, K. (1957). Space and time spectra of stationary stochastic waves, with special reference to microtremors, *Bull. Earthq. Res. Ins.* **35**, 415–457.
- Ammon, C. J., and J. E. Vidale (1993). Tomography without rays, *Bull. Seismol. Soc. Am.* **83**, no. 2, 509–528.
- Amoroso, O., G. Festa, P. Bruno, L. D'Auria, G. De Landro, V. Di Fiore, and A. Zollo (2017). Integrated tomographic methods for seismic imaging and monitoring of volcanic caldera structures and geothermal areas, *J. Appl. Geophys.* **156**, 16–30.
- Assimakis, D., C. Ledezma, G. Montalva, A. Tassara, G. Mylonakis, and R. Boroschek (2012). Site effects and damage patterns, *Earthq. Spectra* **28** (suppl. 1), 55–74.
- Bastías, N., and G. Montalva (2016). Chile strong ground motion flatfile, *Earthq. Spectra* **32**, no. 4, 2549–2566.
- Bensen, G. D., M. H. Ritzwoller, M. P. Barmin, A. L. Levshin, F. Lin, M. P. Moschetti, N. M. Shapiro, and Y. Yang (2007). Processing seismic ambient noise data to obtain reliable broad-band surface wave dispersion measurements, *Geophys. J. Int.* **169**, no. 3, 1239–1260.
- Brenguier, F., N. M. Shapiro, M. Campillo, A. Nercessian, and V. Ferrazzini (2007). 3-D surface wave tomography of the Piton de la Fournaise volcano using seismic noise correlations, *Geophys. Res. Lett.* **34**, no. 2, 2–6, doi: [10.1029/2006GL028586](https://doi.org/10.1029/2006GL028586).
- Cabas, A. (2016). Improvements to the assessment of site-specific seismic hazards, *Ph.D. Thesis*, Department of Civil and Environmental Engineering, Virginia Polytechnic Institute and State University.
- Chávez-García, F. J., and M. Rodríguez (2007). The correlation of microtremors: Empirical limits and relations between results in frequency and time domains, *Geophys. J. Int.* **171**, no. 2, 657–664.
- Chávez-García, F. J., M. Rodríguez, and W. R. Stephenson (2005). An alternative approach to the SPAC analysis of microtremors: Exploiting stationarity of noise, *Bull. Seismol. Soc. Am.* **95**, no. 1, 277–293.
- Cheng, F., J. Xia, Y. Xu, Z. Xu, and Y. Pan (2015). A new passive seismic method based on seismic interferometry and multichannel analysis of surface waves, *J. Appl. Geophys.* **117**, 126–135.
- Delorey, A. A., and J. E. Vidale (2011). Basin shear-wave velocities beneath Seattle, Washington, from noise-correlation Rayleigh waves, *Bull. Seismol. Soc. Am.* **101**, no. 5, 2162–2175.
- Ekström, G., G. A. Abers, and S. C. Webb (2009). Determination of surface-wave phase velocities across USArray from noise and Aki's spectral formulation, *Geophys. Res. Lett.* **36**, no. 18, 5–9.
- Galli, C. (1967). Geología urbana y suelos de fundación de Concepción y Talcahuano, *Informe final del proyecto de investigación N°75 de la Comisión de Investigación Científica de la Universidad de Concepción*, Concepción, Chile (in Spanish).
- Hannemann, K., C. Papazachos, M. Ohrnberger, M. Anthymidis, and A. Lontsi (2012). 3D V_S modeling from high-frequency ambient noise tomography: The case of northern Mygdonia basin, Euroseistest area (northern Greece), *Second European Conf. on Earthquake Engineering and Seismology*, Istanbul, Turkey, 25–29 August 2014, 1–3.
- Hannemann, K., C. Papazachos, M. Ohrnberger, A. Savvaidis, M. Anthymidis, and A. M. Lontsi (2014). Three-dimensional shallow structure from high-frequency ambient noise tomography: New results for the Mygdonia basin-Euroseistest area, northern Greece, *J. Geophys. Res.* **119**, no. 6, 4979–4999.
- Hill, D. P. (2010). Surface-wave potential for triggering tectonic (nonvolcanic) tremor-corrected, *Bull. Seismol. Soc. Am.* **102**, no. 6, 2337–2355.
- Kissling, E. (1988). Geotomography with local earthquake data, *Rev. Geophys.* **26**, no. 4, 659–698.
- Kugler, S., T. Bohlen, T. Forbriger, S. Bussat, and G. Klein (2007). Scholte-wave tomography for shallow-water marine sediments, *Geophys. J. Int.* **168**, no. 2, 551–570.
- Larose, E., A. Derode, M. Campillo, and M. Fink (2004). Imaging from one-bit correlations of wideband diffuse wave fields, *J. Appl. Phys.* **95**, no. 12, 8393–8399.
- Leyton, F., G. Montalva, and P. Ramírez (2012). A preliminary study of seismic microzonation of Concepción based on microtremors, geology and damages patterns, *Obras Proy.* no. 11, 40–46 (in Spanish).
- Long, L. T., and A. H. Kocagözü (2001). Surface-wave group-velocity tomography for shallow structures, *J. Environ. Eng. Geophys.* **6**, no. 2, 71–81.
- Midorikawa, S., H. Yamanaka, K. Chimoto, R. Riddell, H. Miura, and K. Saguchi (2014). Evaluation of site effects on strong-motion records in Concepción during the 2010 Maule, Chile, earthquake, *Bull. Seismol. Soc. Am.* **104**, no. 5, 2503–2511.
- Montalva, G. A., F. J. Chávez-García, A. Tassara, and D. Jara (2016). Site effects and building damage characterization in Concepción after the M_w 8.8 Maule earthquake, *Earthq. Spectra* **32**, no. 3, 1469–1488.
- Moschetti, M. P., M. H. Ritzwoller, and N. M. Shapiro (2007). Surface wave tomography of the western United States from ambient seismic noise: Rayleigh wave group velocity maps, *Geochim. Geophys. Geosys.* **8**, no. 8, 1–10.
- Oliver, M. A., and R. Webster (2015). *Basic Steps in Geostatistics: The Variogram and Kriging*, Springer, New York, New York.

- Picozzi, M., S. Parolai, D. Bindi, and A. Strollo (2009). Characterization of shallow geology by high-frequency seismic noise tomography, *Geophys. J. Int.* **176**, 164–174.
- Pilz, M., S. Parolai, M. Picozzi, and D. Bindi (2012). Three-dimensional shear wave velocity imaging by ambient seismic noise tomography, *Geophys. J. Int.* **189**, 501–512.
- Pilz, M., S. Parolai, M. Stupazzini, R. Paolucci, and J. Zschau (2011). Modelling basin effects on earthquake ground motion in the Santiago de Chile basin by a spectral element code, *Geophys. J. Int.* **187**, 929–945.
- Poblete, M., and R. Dobry (1968). Modelo dinámico del subsuelo de Concepción, *Rev. IDIEM* **7**, no. 3, 111–136 (in Spanish).
- Rojas, I. (2014). Reología y fábrica de la mineralización primaria, yacimiento el teniente, *Memoria de título Geólogo*, Departamento de Geología, Universidad de Chile, Santiago, Chile (in Spanish).
- Roux, P., K. G. Sabra, W. A. Kuperman, and A. Roux (2005). Ambient noise cross correlation in free space: Theoretical approach, *J. Acoust. Soc. Am.* **117**, 79–84.
- Ruiz, S., and G. R. Saragoni (2009). Free vibration of soils during large earthquakes, *Soil Dynam. Earthq. Eng.* **29**, no. 1, 1–16.
- Sabra, K. G., P. Gerstoft, P. Roux, W. A. Kuperman, and M. C. Fehler (2005). Extracting time-domain Green's function estimates from ambient seismic noise, *Geophys. Res. Lett.* **32**, no. 3, 1–5.
- Sabra, K. G., P. Roux, and W. A. Kuperman (2005). Emergence rate of the time-domain Green's function from the ambient noise cross-correlation function, *J. Acoust. Soc. Am.* **118**, no. 6, 3524–3531.
- Sambridge, M. (1999). Geophysical inversion with a neighbourhood algorithm—I. Searching a parameter space, *Geophys. J. Int.* **138**, 479–494.
- Shapiro, N. M., M. Ritzwoller, and G. Bensen (2006). Source location of the 26 sec microseism from cross-correlations of ambient seismic noise, *Geophys. Res. Lett.* **33**, no. 18, 1–5.
- Shirzad, T., and Z. H. Shomali (2014a). Shallow crustal structures of the Tehran basin in Iran resolved by ambient noise tomography, *Geophys. J. Int.* **196**, no. 2, 1162–1176.
- Shirzad, T., and Z.-H. Shomali (2014b). Extracting seismic body and Rayleigh waves from the ambient seismic noise using the rms-stacking method, *Seismol. Res. Lett.* **86**, no. 1, 173–180.
- Snelson, C. M., T. M. Brocher, K. C. Miller, T. L. Pratt, and A. M. Trehu (2007). Seismic amplification within the Seattle basin, Washington state: Insights from SHIPS seismic tomography experiments, *Bull. Seismol. Soc. Am.* **97**, 1432–1448.
- Snieder, R. (2004). Extracting the Green's function from the correlation of coda waves: A derivation based on stationary phase, *Phys. Rev. E* **69**, no. 4, 046610.
- Szanyi, G., Z. Grácz, E. Györi, Z. Kaláb, and M. Lednická (2016). Ambient seismic noise tomography of a Loess high bank at Dunaszekcső (Hungary), *Pure Appl. Geophys.* **173**, no. 8, 2913–2928.
- Thomson, W. T. (1950). Transmission of elastic waves through a stratified solid medium, *J. Appl. Phys.* **21**, no. 2, 89–93, doi: [10.1063/1.1699629](https://doi.org/10.1063/1.1699629).
- Tukey, J. E. (1974). Introduction to today's data analysis, *Proc. of the Conf. on Critical Evaluation of Chemical and Physical Structural Information*, Washington, D.C., 24–29 June 1973, 3–14.
- Vivallos, J., P. Ramirez, and A. Fonseca (2010). Microzonificación Sísmica de la Ciudad de Concepción, *Región del Biobío, Servicio Nacional de Geología y Minería. Carta Geológica de Chile*, Serie Geología Ambiental Series, **17** (in Spanish).
- Wathelet, M. (2008). An improved neighborhood algorithm: Parameter conditions and dynamic scaling, *Geophys. Res. Lett.* **35**, no. 9, 1–5.
- Weaver, R., and O. Lobkis (2002). On the emergence of the Green's function in the correlations of a diffuse field: Pulse-echo using thermal phonons, *Ultrasonics* **40**, nos. 1/8, 435–439.
- Wessel, P., W. H. F. Smith, R. Scharroo, J. F. Luis, and F. Wobbe (2013). GMT 5: A major new release of the generic mapping tools, *Eos Trans. AGU* **94**, no. 45, 409–410.
- Yang, Y., M. H. Ritzwoller, A. L. Levshin, and N. M. Shapiro (2007). Ambient noise Rayleigh wave tomography across Europe, *Geophys. J. Int.* **168**, no. 1, 259–274, doi: [10.1111/j.1365-246X.2006.03203.x](https://doi.org/10.1111/j.1365-246X.2006.03203.x).

Departamento de Ingeniería Civil
Universidad de Concepción
Víctor Lamas 1290, Casilla 160-C, Correo 3
4070409 Concepción, Chile
diegoinzunza@udec.cl
(D.A.I.)

Departamento de Ingeniería Civil
Universidad de Concepción
Edmundo Larenas 219, Casilla 160-C, Correo 3
4070409 Concepción, Chile
gmontalva@udec.cl
(G.A.M.)

Centro Sismológico National
University of Chile
Blanco Encalada 2002, Casilla #2777
8370415 Santiago, Chile
leyton@csn.uchile.cl
(F.L.)

Geosciences Department
National University of Colombia
Carrera 30 #45-03
111321 Bogotá, Colombia
gaprieto@unal.edu.co
(G.P.)

Geophysics Department
University of Chile
Blanco Encalada 2002, Casilla #2777
8370415 Santiago, Chile
sruiz@dgf.uchile.cl
(S.R.)

Manuscript received 23 February 2018;
Published Online 11 December 2018